

Generating Multiple Hypotheses for Human 3D Pose Consistent with 2D Joint Detections

Ehsan Jahangiri
Johns Hopkins University
Baltimore, USA
ejahang1@jhu.edu

Alan L. Yuille
Johns Hopkins University
Baltimore, USA
alan.yuille@jhu.edu

Abstract

We propose a method to generate multiple hypotheses for human 3D pose all of them consistent with the 2D detection of joints in a monocular RGB image. To generate these pose hypotheses we use a novel generative model defined in the space of anatomically plausible 3D poses satisfying the joint angle limits and limb length ratios. The proposed generative model is uniform in the space of anatomically valid poses and as a result, does not suffer from the dataset bias in existing motion capture datasets such as Human3.6M (H36M), HumanEva, and CMU MoCap. A good model that spans the full variability of human pose and generalizes to unseen poses must be compositional i.e. produce a pose by combining parts. Our model is flexible and compositional and consequently can generalize to every plausible human 3D pose since it is only limited by physical constraints. We discuss sampling from this model and use these samples to generate multiple diverse human 3D pose hypotheses given the 2D detection of joints. We argue that generating multiple pose hypotheses from a monocular RGB image is more reasonable than generating only a single 3D pose given the depth ambiguity and the uncertainty caused by occlusion and imperfect 2D joint detection. To support this argument, we have performed empirical evaluation on the popular Human3.6M dataset that confirms that most often, at least one of our pose hypotheses is closer to the true 3D pose compared to the estimated pose by other recent baseline methods for 3D pose reconstruction from monocular RGB images. The idea of generating multiple consistent and valid pose hypotheses can give rise to a new line of future work that has not previously been addressed in the literature.

1. Introduction

Estimating the 3D pose configurations of complex articulated objects such as humans from monocular RGB images is a challenging problem. There are multiple factors contributing to the difficulty of this critical problem in computer vision: (1) multiple 3D poses can have similar 2D

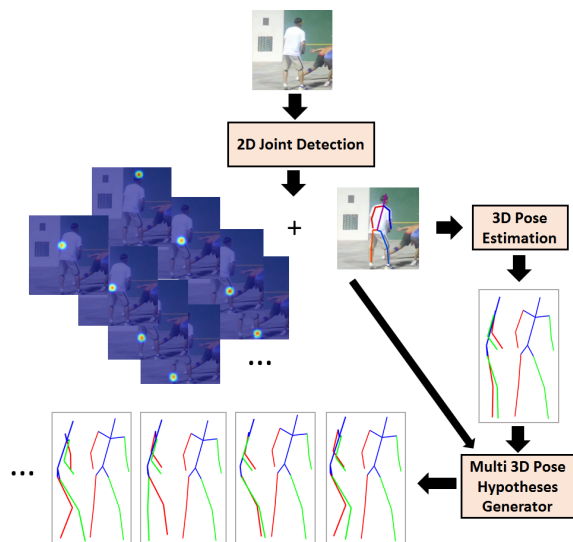


Figure 1: Overview of the proposed “Multi-Pose-Hypotheses” approach. The input monocular image is first passed through a CNN-based joint detector which outputs a set of heatmaps for soft localization of 2D joints. The estimated 2D joints are then passed to a 2D-to-3D pose estimator to obtain an estimate of the 3D torso and the projection matrix. Using the estimated 3D torso, the projection matrix, and the output of the 2D detector we generate multiple 3D pose hypotheses. The generated pose hypotheses (the left-hand-side poses in each gray box) are quite different even though their projections (the right-hand-side poses) are similar and consistent with the output of 2D joint detector.

projections. This renders 3D human pose reconstruction from its projected 2D joints an ill-posed problem; (2) the human motion and pose space is highly nonlinear which makes pose modeling difficult; (3) detecting precise location of 2D joints is challenging due to the variation in pose and appearance, occlusion including both from other people/objects and self-occlusion, and cluttered background. Also, minor errors in the detection of 2D joints can have a large effect on the reconstructed 3D pose. These factors favor a 3D pose estimation system that takes into account

the uncertainties and suggests multiple possible 3D poses. Often in the image, there exist much more detailed information about the 3D pose of a human (such as contextual information and difference in shading/texture due to depth disparity) than the 2D location of the joints. Hence, most of the possible 3D poses consistent with the 2D joint locations can be rejected based on more detailed image information (*e.g.* in an analysis-by-synthesis framework or by investigating the image with some mid-level queries such as “Is the left hand in front of torso?”) or by physical laws (*e.g.* gravity). However, note that we can also imagine scenarios where the image does not contain enough information to rule out or favor one 3D pose configuration over another especially in the presence of occlusion resulting in a level of uncertainty in such cases. In this paper, we focus on generating multiple plausible 3D pose hypotheses which while satisfying humans anatomical constraints, including the joint angle limits and limb length ratios, are still consistent with the output of the 2D joint detector. Figure 1 illustrates an overview of our approach.

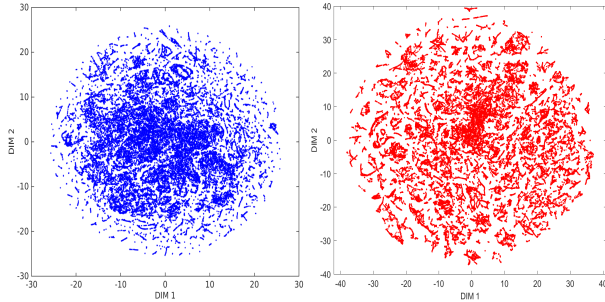
The space of valid human poses is a non-convex complicated space constrained by the anatomical and anthropomorphic limits. A bone never bends beyond certain angles with respect to its parent bone in the kinematic chain and its normalized length, with respect to other bones, cannot be much shorter/longer than standard values. This inspired Akhter and Black [1] to build a motion capture dataset composed of 3D poses of flexible subjects such as gymnasts and martial artists to study the joint angle limits. The statistics of 3D poses in this motion capture dataset is different from the previously existing motion capture datasets such as CMU [13], Human 3.6M [17], and HumanEva [27], because of their intention to explore the joint angle limits rather than performing typical human actions. Figure 2 shows the t-SNE visualization [33] of poses from Akhter&Black motion Capture Dataset (ABCD) versus H36M in two dimensions. One can see that the “ABCD” dataset is more uniformly distributed compared to the H36M dataset. We randomly selected 4 poses from the dense and surrounding sparse areas in the H36M t-SNE map and have shown the corresponding images. One can see that all of the four samples selected from the dense areas correspond to standing poses whereas all of the four samples selected from sparse areas correspond to sitting poses. Training and testing on a similarly biased dataset with excessive repetition of some poses will result in reduced performance on novel or rarely seen poses. For example, we observed that the Deep3D pose estimator network [10] that is regressing directly from the 2D image to the 3D location of the joints performs poorly on poses with bent knees (*i.e.* sitting); this could be expected since the Deep3D network is trained on the H36M dataset which favors some common poses as well as synthetic images with 3D poses generated

by the generative model of Lehrmann et al. [19] trained on previously existing motion capture datasets with bias.

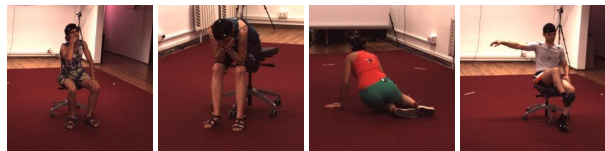
Obviously, any solely data-driven pose estimator learned from a biased dataset that does not cover the full range of motion of human body can suffer from lack of generalization to novel or rarely seen anatomically plausible poses. Note that even though we talked about bias toward certain 3D poses in MoCap datasets the bias can be due to different factors (2D or 3D) *e.g.* we will run experiments that show drastic drop in the performance of Deep3D pose estimator [10] for rotated images which is partly due to insufficient tilted images in the training set. On the other hand, humans can learn from a few examples and still not suppress the rarely seen cases compared to the frequently seen ones. A pose estimator should also be able to handle rarely seen or novel poses equally well. A data-driven compositional model limited only by the physics of the problem, namely the anatomical limits of human body, is a logical approach to prevent the adverse effects of dataset bias. In our multi-hypotheses generation approach, we use the pose-dependent joint angle limits studied in [1] and as a result our method is flexible, unbiased, and constrained only by anatomical properties.

The contributions of this paper are as follows. We propose a novel generative model for human 3D poses uniform in the space of *physically valid* poses (satisfying constraints by Akhter and Black [1]) that does not suffer from dataset bias since it is constrained only by human body anatomical limits. Assuming the provision of a 2D joint detector, we introduce a method to generate multiple diverse and anatomically valid 3D pose hypotheses consistent with the 2D detector’s output using our generative model. To the best of our knowledge we are the first to address and generate multiple valid 3D poses consistent with 2D joint detections under different ambiguities (including depth ambiguity) for monocular images. We believe that our suggested idea of generating multiple pose hypotheses will give rise to a new line of future work that has not previously been addressed in the literature. Our approach to generate multiple pose hypotheses does not depend on any specific 2D/3D pose estimator. However, as proof of concept we used the “Stacked Hourglass” 2D joint detector [21] and the 2D-to-3D pose estimators of Akhter&Black [1] and Zhou et al. [39] to estimate the 3D torso and projection matrix.

We review related works in subsection 1.1. In section 2, we propose our approach based on a generative model on human 3D poses to sample both unconditional and conditional to the output of a 2D joint detector. Our experimental results and comparison with multiple 3D pose estimation baselines are given in section 3. We conclude our paper with a discussion in section 4.



Random Samples from the **Dense** Area of the H36M t-SNE map.



Random Samples from the **Sparse** Area of the H36M t-SNE map.

Figure 2: Top: t-SNE visualization of poses from the H36M (left-hand-side in blue) and ABCD (right-hand-side in red). The images corresponding to the random selection of poses from the dense (second row) and sparse (third row) area of the H36M t-SNE map clearly confirm the dataset bias toward standing poses compared to sitting poses.

1.1. Related Work

There are quite a few works in the human pose estimation literature that are directly or indirectly related to our work. Reviewing the entire literature is obviously beyond the scope of this paper. Several areas of research are related to our work such as 2D joint detection, 3D pose estimation, and generative 3D pose modeling. In this paper, we assume that the 2D detection of joints are provided and we use a baseline 2D-to-3D pose estimator to obtain an estimate of the 3D torso and the projection matrix. Due to the advancements made by deep neural networks, the most recent works on 2D joint detection are based on convolutional neural networks (CNN). Toshev and Szegedy [32] proposed the first 2D joint detector based on CNNs to directly regress the x and y coordinates of joints and achieved superior performance compared to the traditional hand-crafted feature based methods [26, 38, 14]. Researchers have also employed graphical models in conjunction with CNNs to incorporate structure [11, 31, 12, 37, 36]. Recent works [35, 21, 8] instead design more powerful deep network architectures with large receptive fields to learn the long-range spatial relationships between different parts without using graphical models and achieve state-of-the-art performance on several 2D human pose estimation bench-

marks. We use the “Stacked Hourglass” network [21] for 2D joint detection in this paper. On the other hand, most of the 3D pose estimation methods use sparse coding based on an overcomplete dictionary of basis poses to represent a 3D pose and fit the 3D pose projection to the 2D joint detections [24, 34, 1, 39, 40]. Bogo et al. [7] try to fit the projection of human 3D shape to the 2D joints and show an improvement in performance. However, there is no guarantee that the samples taken from their Gaussian Mixture Model (GMM) are physically plausible. Some works [10, 25] use synthetic data and train neural networks to directly predict 3D poses. Discriminative approaches for 3D structure prediction such as [10] are usually very sensitive to data manipulation compared to generative approaches. As a test to show this we generated two datasets by rotating images from H36M and passed them through the regression network of Chen et al. [10]; the predicted poses from these rotated images did not usually correspond to valid human poses satisfying anthropomorphic constraints as there is no guarantee that the 3D poses estimated by a discriminative regression network are valid. On the other hand, it has been shown that the deep networks are very effective and more robust at detecting 2D templates (compared to 3D structures) such as human 2D body parts in images as also approved by our test using the HourGlass network on rotated images. The dataset bias (toward certain 2D appearances or 3D poses) can possibly hurt 2D joint detection as well but we did not observe as much adverse effect of dataset bias (rotation bias in this case) in 2D joint detection compared to direct 3D pose regression.

There are different sources of ambiguity in estimating human 3D pose from a monocular image. Simo-Serra et al. [30] propagate the error in the estimation of 2D joint locations (modeled using Gaussian distributions) into the weights of dictionary elements in a sparse coding framework; then by sampling the weights, some 3D pose samples are generated and sorted based on the SVM score on joint distance features. Their approach does not guarantee that the joint angle constraints are satisfied and do not address the depth ambiguity. Pose estimation through sampling is done in a number of previous works [9, 28, 2, 5, 6]. However, the samplings performed by these works are for purposes different from our goal to generate multiple diverse valid pose hypotheses. For example, Burenus et al. [9] generate some sparsely distributed samples in a multi-view framework and investigate the feasibility of dynamic programming in a much smaller space to estimate a single pose. Sigal et al. [28] use non-parametric belief propagation in an iterative fashion for inference where the messages are calculated through sampling based on 2D joint candidates in multiple views. Amin et al. [2] use a mixture of pictorial structures and perform inference in two stages where the first stage reduces the search space for the second stage in-

ference by generating samples for the 2D location of each part. Belagiannis et al. [5] also assume a multi-view framework and create a set of 3D body part hypotheses for faster inference by triangulation of corresponding 2D body joints sampled from the posteriors of 2D body part detectors in all camera views pairs. We know that acquiring information from multiple views results in much less ambiguity (more specifically depth ambiguity) compared to a single-view scenario that we assume. However, all of these works output only one 3D pose despite the pose uncertainty. To the best of our knowledge there is no work in the literature that aims at generating multiple 3D pose hypotheses consistent with detected 2D joints in a monocular image under different ambiguities including depth. One interesting work is the “Posebit” by Pons-Moll et al. [23] that can retrieve pose candidates from a MoCap dataset of 3D poses given answers to some mid-level queries such as “Is the right hand in front of torso?” using decision trees (using a strategy similar to [18]). This approach is heavily dependent on the choice of MoCap dataset and cannot generalize to unseen poses; Posebit also does not exploit the recent advances in 2D pose estimation using deep neural networks. However, their approach of asking mid-level questions in addition to the output of 2D joint detectors can be useful to rule out some of our generated pose hypotheses. Obviously there is much more information in an image than the 2D location of joints. It is also worth mentioning two other related works of Simo-Serra et al. [29] and Lehrmann et al. [19]. Simo-Serra et al. [29] model the 2D and 3D poses jointly in a Bayesian framework by integrating a generative model and discriminative 2D part detectors based on HOGs. Lehrmann et al. [19] learn a generative model from the H36M MoCap dataset whose graph structure (not a Kinematic chain) is learned using the Chow-Liu algorithm.

In this paper, we focus on generating multiple valid and consistent pose hypotheses and postpone ruling out the pose hypotheses beyond their consistency with 2D joint detections to future work.

2. The Proposed Method

Since our multi-hypotheses generation approach is closely related to the joint-angle validity constraints used in [1], we find it useful to review this work briefly as follows. To represent the human 3D pose by its joints let \mathbf{X} denote the matrix corresponding to P kinematic joints in the 3D space namely $\mathbf{X} = [\mathbf{X}_1 \dots \mathbf{X}_P] \in \mathcal{X} \subset \mathbb{R}^{3 \times P}$ where \mathcal{X} denotes the space of valid human poses. Akhter&Black [1] (similar to [24, 39]) assumed that all of the 2D joints are observed and estimated the 3D pose by solving the following optimization problem:

$$\min_{\omega, s, \mathbf{R}} C_r + C_p + \beta C_l, \quad (1)$$

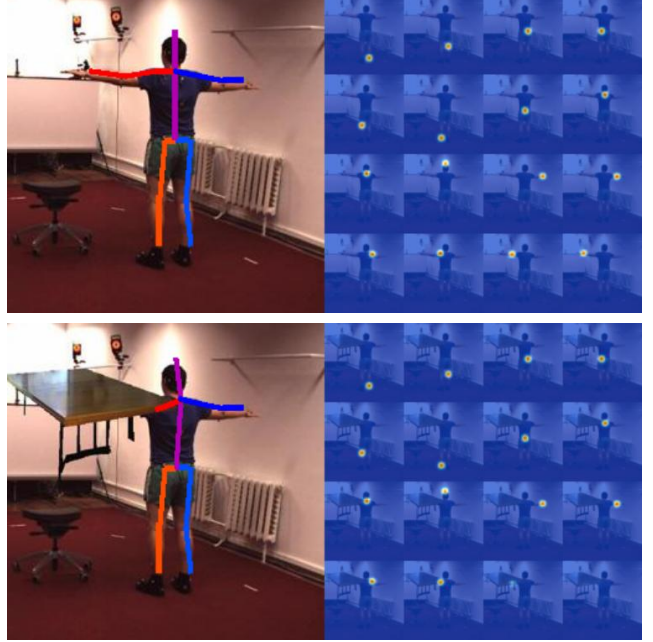


Figure 3: “Stacked Hourglass” 2D joint detector [21] in the absence and presence of occlusion. On the right-hand-side of each image are the corresponding heatmaps for joints.

where, C_r is a measure of fitness between the estimated 2D joints $\hat{\mathbf{x}} \in \mathbb{R}^{2 \times P}$ and the projection and translation of estimated 3D pose $\hat{\mathbf{X}} = [\hat{\mathbf{X}}_1 \dots \hat{\mathbf{X}}_P] \in \mathbb{R}^{3 \times P}$ to the 2D image coordinate system in a weak perspective camera model (orthographic projection) with scaling factor $s \in \mathbb{R}^+$, rotation $\mathbf{R} \in SO(3)$, and translation $\mathbf{t} \in \mathbb{R}^{2 \times 1}$, defined as:

$$C_r = \sum_{i=1}^P \|\hat{\mathbf{x}}_i - s\mathbf{R}_{1:2} \hat{\mathbf{X}}_i + \mathbf{t}\|_2^2, \quad (2)$$

where, $\mathbf{R}_{1:2}$ denotes the first two rows of the rotation matrix. Note that if the origin of the 3D world coordinate system gets mapped to the origin of the 2D image coordinate system then $\mathbf{t} = \mathbf{0}$; this is usually implemented by centering the 2D and 3D poses. Authors used a sparse representation of the 3D poses similar to [24] where the 3D pose is represented by a sparse linear combination of bases selected using the Orthogonal Matching Pursuit (OMP) algorithm [20] from an overcomplete dictionary of pose atoms, namely $\hat{\mathbf{X}} = \mu + \sum_{i \in \mathcal{I}^*} \omega_i \mathbf{D}_i$, where μ is the mean pose obtained by averaging poses from the CMU motion capture dataset [13] and \mathcal{I}^* denotes the indices of selected bases using OMP with weights ω_i . An overcomplete dictionary of bases was built by concatenating PCA bases from poses of different action classes in the CMU dataset after bone length normalization and Procrustes aligned. The term C_l in (1) penalizes the difference between the squares of the estimated i^{th} bone length l_i and the normalized mean bone length \bar{l}_i i.e., $C_l = \sum_{i=1}^N |l_i^2 - \bar{l}_i^2|$ with weight β . The sec-

ond term C_p in (1) is equal to zero if the estimated pose $\hat{\mathbf{X}}$ has valid joint angles for limbs and infinity otherwise. According to [1] a pose has valid joint angles if the upper arms/legs' joint angles map to a 1 in the corresponding occupancy matrix (learned from the ABCD dataset) and the lower arms/legs satisfy two conditions that prevent these bones from bending beyond feasible joint-angle limits (constraints in (4) and (5)).

2.1. Our Approach

As we mentioned earlier, 3D pose estimation from 2D landmark points in monocular RGB images is inherently an ill-posed problem because of losing the depth information. There can be multiple valid 3D poses with similar 2D projection even if all of the 2D joints are observed (see Figure 1). The uncertainty and number of possible valid poses can further increase if some of the joints are missing. The missing joints scenario is more realistic because it happens when either these joints exist in the image but are not confidently detected, due to occlusion and clutter, or do not exist within the borders of the image *e.g.* when only the upper body is visible similar to images from the FLIC dataset [26]. It is observed that thresholding the confidence score obtained from some deep 2D joint detectors (*e.g.* [21, 22, 16]) can be reasonably used as an indicator for the confident detection of a joint. Figure 3 shows the output of “Stacked Hourglass” 2D joint detector [21] in the absence and presence of a table occluder segmented out from the Pascal VOC dataset [15] and pasted on the left hand of the human subject. On the right-hand-side of each image is shown the heatmap for each joint. It can be seen that the level of the two heatmaps corresponding to the left elbow and left wrist drop after placing the table occluder on the left hand. Newell et al. [21] used the heatmap mean as a confidence measure for detection and threshold it at 0.002 to determine visibility of a joint. Obviously, invisibility of some joints in the image can result in multiple hallucinations for the 2D/3D locations of the joints. Let S_o and S_m denote the set of observed and missing joints, respectively. We have $S_o \cap S_m = \emptyset$ and $S_o \cup S_m = \{1, 2, \dots, P\}$, and let $\alpha = \{\alpha_i\}_{i \in S_o}$ denote a set of normalized joint scores from the 2D joint detectors such that $\frac{1}{|S_o|} \sum_{i \in S_o} \alpha_i = 1$. The missing joints are detected by comparing the confidence score of 2D joint detector with a threshold (0.002 in the case of using Hourglass). For the case of missing joints, we modify the fitness measure in (2) to:

$$C_r = \sum_{i \in S_o} \alpha_i \|\hat{\mathbf{x}}_i - s\mathbf{R}_{1:2} \hat{\mathbf{X}}_i + \mathbf{t}\|_2^2. \quad (3)$$

The scores are normalized because they have to be in a comparable range with respect to the C_l term in (1) otherwise either C_r is suppressed/ignored in the case of very small confidence scores or the same happens to C_l in the case of very

large scores. For example, if the mean of heatmaps from the Hourglass joint detector are directly (without normalization) used as scores the C_r term will be drastically suppressed since the heatmaps are full of close-to-zero values. Note that the optimization problem in (1) with the updated C_r term according to (3) still outputs a full 3D pose even under missing joints scenario because the 3D pose is constructed by a linear combination of full body basis. However, there is no reason that the output 3D pose should have a close to correct 2D projection due to the missing joint ambiguity added to the depth ambiguity. Optimizing C_r is a non-convex optimization problem over the 3D pose and projection matrix. To obtain an estimate of the 3D torso and projection matrix, we tried both iterating between optimizing over the projection matrix and 3D pose used in [1] as well as the convex relaxation method in [39] as will be presented in the experimental results section. To generate multiple diverse 3D pose hypotheses consistent with the output of 2D joint detector, we cluster samples from a conditional distribution given the collected 2D evidence. For this purpose, we follow a rejection sampling strategy. Before discussing conditional sampling in subsection 2.3 we describe unconditional sampling as follows.

2.2. Unconditional Sampling

Given the rigidity of human torso compared to the limbs (hands/legs), the joints corresponding to the torso including thorax, left/right hips, and left/right shoulders can be represented using a small size dictionary after an affine transformation/normalization. Hence, to sample the torso, we can randomly select one of the elements of this dictionary. Given the torso, the upper arms/legs and head are anatomically restricted to be within certain angular limits. Akhter&Black [1] calculated these plausible angular regions for the upper arms/legs and head using an occupancy matrix. The occupancy matrix is a binary matrix that assigns 1 to a discretized azimuthal θ and polar ϕ angle if these angles are anatomically plausible and 0 otherwise. These angular positions are calculated in the local Cartesian coordinate system whose two axis are the “backbone” vector and either the “right shoulder \rightarrow left shoulder” vector (for the upper arms and head) or the “right hip \rightarrow left hip” vector (for the upper hips). To generate samples for the upper arms/legs and head we just need to take samples from the occupancy matrix at places where the value is 1 and get the corresponding azimuthal and polar angles. Given the azimuthal and polar angles of the head we just need to travel in this direction for the length of the head; we do the same for the length of upper arms and legs to reach the elbows and knees, respectively. The normalized length of the bones is sampled from a Beta distribution with limited range under the constraint that similar bones have similar length *e.g.* both upper arms have the same length.

According to [1], the lower arm/leg bone $\mathbf{b}_{p_1 \rightarrow p_2} = \mathbf{X}_{p_2} - \mathbf{X}_{p_1}$, where p_2 and p_1 respectively correspond to either “wrist and elbow” or “ankle and knee” is at a plausible angle if it satisfies two constraints. The first constraint is:

$$\mathbf{b}^\top \mathbf{n} + d < 0, \quad (4)$$

where \mathbf{n} and d are functions of the azimuthal θ and polar ϕ angles of their parent bone namely the upper arm or leg (resulting in pose-dependent joint angle limits) learned from the ABCD dataset. The above inequality defines a separating plane, with normal vector \mathbf{n} and distance from origin d , that attempts to prevent the wrist and ankle from bending in a direction that is anatomically impossible. Obviously, for a very negative offset vector d the (4) constrain is always satisfied. Therefore, during learning of \mathbf{n} and d the second norm of d is minimized, namely $\min_{\mathbf{n}, d} \|\mathbf{d}\|_2$ s.t. $\mathbf{B}^\top \mathbf{n} < -d\mathbf{1}$, where \mathbf{B} is a matrix built by column-wise concatenation of all \mathbf{b} instances in the ABCD dataset whose parents are at the same θ and ϕ angular location. The second constraint to satisfy is that the projection of normalized \mathbf{b} (to unit length) onto the separating plane using the orthonormal projection matrix $\mathbf{T} = [\mathbf{T}_1; \mathbf{T}_2; \mathbf{T}_3]$, whose first row \mathbf{T}_1 is along \mathbf{n} , has to fall inside of a bounding box with bounds $[bnd_1, bnd_2]$ and $[bnd_3, bnd_4]$, namely:

$$\begin{aligned} bnd_1 &\leq \mathbf{T}_2 \mathbf{b} / \|\mathbf{b}\|_2 \leq bnd_2, \\ bnd_3 &\leq \mathbf{T}_3 \mathbf{b} / \|\mathbf{b}\|_2 \leq bnd_4, \end{aligned} \quad (5)$$

where, bounds bnd_1 , bnd_2 , bnd_3 , and bnd_4 are learned from the ABCD dataset. To generate a sample \mathbf{b} that satisfies the above constraints, we first generate two random values $u_2 \in [bnd_1, bnd_2]$ and $u_3 \in [bnd_3, bnd_4]$ and set $u_1 = \sqrt{\max(1 - u_2^2 - u_3^2, 0)}$. We then generate two candidates $\mathbf{u}^\pm = (\pm u_1, u_2, u_3) / \|(u_1, u_2, u_3)\|_2$ from which only one can be on the valid side of the separating plane satisfying (4). To check, we first undo the projection and normalization by $\mathbf{b}^\pm = l \mathbf{T}^{-1} \mathbf{u}^\pm$, where l is a sample from the bone length distribution on \mathbf{b} . A sample “ \mathbf{b} ” is accepted only if it satisfies (4). Note that similar bones have the same length therefore we sample their length only once for each pose. The prior model can be written as below according to a Bayesian network on the kinematic chain:

$$\begin{aligned} p(\mathbf{X}) &= p(\mathbf{X}_{i \in \text{torso}}) p(\mathbf{X}_{\text{head}} | \mathbf{X}_{i \in \text{torso}}) \times \\ &p(\mathbf{X}_{i \in \text{l/r elbow}} | \mathbf{X}_{i \in \text{torso}}) p(\mathbf{X}_{i \in \text{l/r wrist}} | \mathbf{X}_{i \in \text{l/r elbow}}, \mathbf{X}_{i \in \text{torso}}) \times \\ &p(\mathbf{X}_{i \in \text{l/r knee}} | \mathbf{X}_{i \in \text{torso}}) p(\mathbf{X}_{i \in \text{l/r ankle}} | \mathbf{X}_{i \in \text{l/r knee}}, \mathbf{X}_{i \in \text{torso}}), \end{aligned}$$

where $p(\mathbf{X}_{i \in \text{torso}})$ is the probability of selecting a torso from the torso dictionary which we assumed is uniform. The torso joints $\mathbf{X}_{i \in \text{torso}}$ are used to determine the local coordinate system for the rest of the joints. We have removed

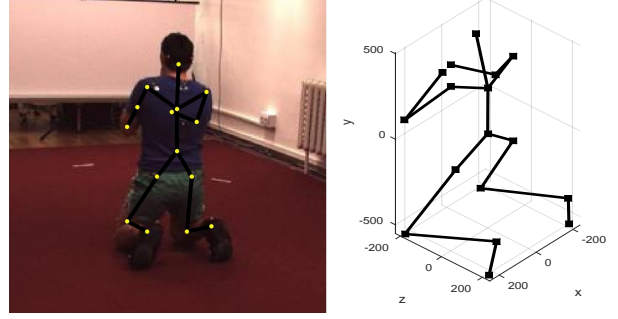


Figure 4: The yellow circles on the left image show the 2D location of detected joints using the “Stacked Hourglass” joint detector [21]. The corresponding ground-truth 3D pose is shown on the right.

torso joints in the equations below for notational convenience. We have:

$$p(\mathbf{X}_i) = \frac{1}{l_{\text{bone}}^2 |\sin(\phi_i)|} p(l_{\text{bone}}) p(\theta_i, \phi_i), \quad (6)$$

for (i, bone) being from (l/r knee, upper leg), (head, neck + head bone), or (l/r elbow, upper arm). The multiplier factor in (6), which is the inverse of Jacobian determinant for a transformation from the Cartesian to spherical coordinate system, is to ensure that the left side sums up to one if $\int_l \int_\theta \int_\phi p(l) p(\theta, \phi) d\phi d\theta dl = 1$, since $dx dy dz = l^2 |\sin(\phi)| dl d\theta d\phi$. For lower limbs we have:

$$p(\mathbf{X}_i | \mathbf{X}_{pa(i)}) \propto p(l_{\text{bone}}) \mathbf{1}_{\text{valid}}(\mathbf{X}_i, \mathbf{X}_{pa(i)}) \quad (7)$$

where $(i, pa(i), \text{bone})$ is from (l/r wrist, l/r elbow, forearm) or (l/r ankle, l/r knee, lower leg), and $\mathbf{1}_{\text{valid}}(\mathbf{X}_i, \mathbf{X}_{pa(i)})$ is an indicator function that nulls the probability of configurations whose angles does not satisfy the constraints in (4) and (5) for $\mathbf{b} = \mathbf{X}_i - \mathbf{X}_{pa(i)}$. Conditional sampling is carried out by rejection sampling as discussed in the next subsection.

2.3. Conditional Sampling

We run a 2D joint detector on the input image I and get an estimate of the 2D joint locations $\hat{\mathbf{x}}$ with scores α . Then, to obtain a reasonable estimate of torso $\hat{\mathbf{X}}_{i \in \text{torso}}$ and camera parameters namely $(\hat{\mathbf{R}}, \hat{\mathbf{t}}, \hat{s})$, we run a 2D-to-3D pose estimator modified to handle missing joints (we used modified [1] and [39]). Note that we can run any 2D joint detector that estimates 2D joint locations $\hat{\mathbf{x}}$ and their scores α and any 2D-to-3D pose estimator that can handle missing joints in the initial stage. We then assume that the estimated camera parameters and $\hat{\mathbf{X}}_{i \in \text{torso}}$ are accurately estimated and keep them fixed. Note that the human torso does not vary much compared to the whole body pose. We do not include the estimated camera parameters and 3D torso

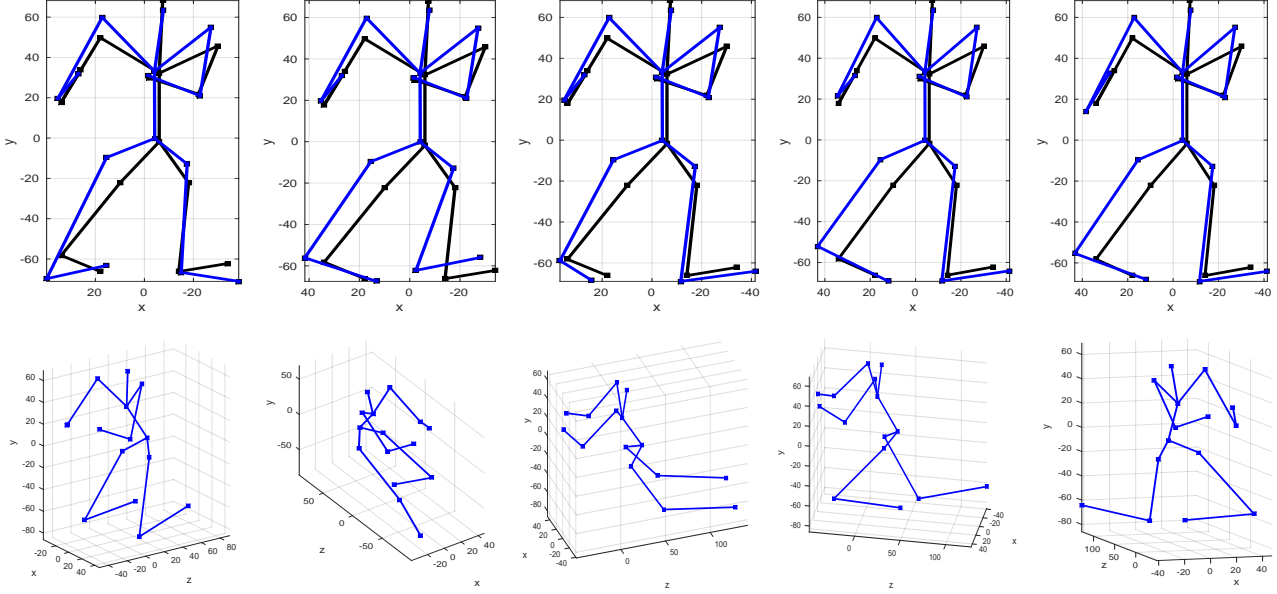


Figure 5: Generation of five diverse 3D pose hypotheses consistent with the 2D joint detections output by “Stacked Hourglass” [21]. The first row shows the 2D detections (black skeleton) and the projection of 3D pose hypotheses (blue skeleton). The corresponding 3D pose hypotheses are shown on the second row right below their 2D projections from a different viewpoint. It can be seen that the generated 3D pose hypotheses are quite different even though their projections are similar and consistent with the 2D detections.

in our formulation below for notational convenience. From Bayes rule, we get the following conditional distribution:

$$p(\mathbf{X}|\hat{\mathbf{x}}, \alpha) \propto p(\mathbf{X}) p(\hat{\mathbf{x}}, \alpha|\mathbf{X}). \quad (8)$$

We define:

$$p(\hat{\mathbf{x}}, \alpha|\mathbf{X}) \propto \prod_{i \in \text{limb} \cap S_o} \mathbf{1}(\|\hat{\mathbf{x}}_i - \hat{\mathbf{s}} \hat{\mathbf{R}}_{1:2} \mathbf{X}_i + \hat{\mathbf{t}}\|_2 < \tau_i)$$

where $\mathbf{1}(\cdot)$ is the indicator function depending on the acceptance threshold on the 2D distance between detected joints and the projected 3D pose defined by $\tau_i = 0.25 \hat{s} \bar{l}_{\text{limb}} / \alpha_i$, where \bar{l}_{limb} is the mean limb length, \hat{s} is the estimated scaling factor, α_i is the i^{th} joint normalized score, and the factor 0.25 was selected empirically. The likelihood function defined above accepts prior (unconditional) samples $\mathbf{X}^{(q)} \sim p(\mathbf{X})$ whose projected joints to the image coordinate system are within a distance not greater than thresholds τ_i from detected limb joints. The inverse proportion of the threshold to the confidence α_i allows acceptance in a larger area if the confidence score is smaller for the i^{th} limb joint and therefore considering the 2D joint detection uncertainty. Note that there is no indicator function in the likelihood function for the missing limb joints which allows acceptance of all anatomically plausible samples for limb joints from S_m . Our posterior sampling follows a rejection sampling framework in which an anatomically plausible sample from the prior $p(\mathbf{X})$ is accepted if its projection results in limb joints

that satisfies $\prod_{i \in \text{limb} \cap S_o} \mathbf{1}(\|\hat{\mathbf{x}}_i - \hat{\mathbf{s}} \hat{\mathbf{R}}_{1:2} \mathbf{X}_i + \hat{\mathbf{t}}\|_2 < \tau_i) = 1$ and rejected otherwise. We next discuss diversifying the conditional samples if we want to have only a few number of representatives (hypotheses).

2.4. Generating Diverse Hypotheses

The diversification is implemented in two stages: (I) we sampled the occupancy matrix at 15 equidistant azimuth and 15 equidistant polar angles for the upper limbs and accept the samples if the occupancy matrix had a 1 at these locations. For the lower limbs, we sampled 5 equidistant points along each u_2 and u_3 directions between $[bnd_1, bnd_2]$ and $[bnd_3, bnd_4]$, respectively. (II) To generate fewer number of pose hypothesis, we use the kmeans++ algorithm [4] to cluster the posterior samples into a desired number of diverse clusters and take the nearest neighbor 3D pose sample to each centroid as one hypothesis. Note that we cannot take the centroids as hypotheses since there is no guarantee that the mean of 3D poses is still a valid 3D pose. Figure 5 shows five hypotheses given the output of Hourglass 2D joint detector for the image and detections shown in Figure 4. In Figure 5, the 2D detection of joints are shown by the black skeleton and the diversified hypotheses that are consistent with the 2D detections are shown by the blue skeletons. It can be seen that even though the 2D projection of these pose hypotheses are very similar, they are quite different in 3D. To generate the pose hypotheses in Figure 5, we estimated the 3D torso and projection matrix

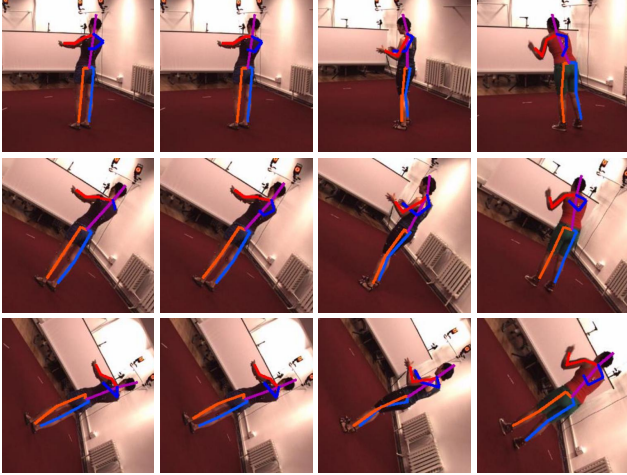


Figure 6: Example images from the original H36M (first row), rotated by 30 (second row) and 60 (third row) degrees datasets and their 2D joint detections.

using [1].

3. Experimental Results

We empirically evaluated the proposed “multi-pose hypotheses” approach on the recently published Human3.6M dataset [17]. The Human3.6M dataset is a large dataset for 3D human sensing which includes millions of 3D human poses with corresponding images from four calibrated cameras. The 3D poses are acquired from a MoCap system providing synchronized videos and 2D-3D pose data. It includes 11 subjects performing 15 different actions such as posing, smoking, sitting and walking. For evaluation, we used images from all 4 cameras and all 15 actions associated with 7 subjects for whom ground-truth 3D poses were provided namely subjects S1, S5, S6, S7, S8, S9, and S11. The original frame rate of videos from Human3.6M dataset is 50 fps and therefore consecutive frames are highly correlated. Hence, we downsampled the video frames and built a dataset of 26385 images with diverse poses. For further evaluation, we also built two rotation datasets by rotating H36M images by 30 and 60 degrees. Figure 6 shows some examples from the original (first row), 30 and 60 degrees rotation (second and third row) datasets with the output of pre-trained Stacked Hourglass model¹ [21] trained on annotated images from the FLIC [26] and MPII Human Pose [3] datasets. It can be seen in these examples (Figure 6) that the 2D detection of joints is quite robust to rotation which shows that the deep networks are quite powerful at 2D detection.

We evaluated the performance by the mean per joint error (millimeter) in 3D by comparing the reconstructed pose

hypotheses against the ground truth. The error was calculated up to a similarity transformation obtained by Procrustes alignment. The results are summarized in Table 1 for various methods and actions. For a fair comparison, the limb length of the reconstructed poses from all methods were scaled to match the limb length of the ground-truth pose (Table 3 shows the mean per joint error when no bone length matching has been performed). The bone length matching obviously lowers the mean joint errors but makes no difference in our comparisons. One can see that the best (lowest Euclidean distance from the ground-truth pose) out of only 5 generated hypotheses by using [1] as baseline for 3D torso and projection matrix estimation is considerably better than the single 3D pose output by [1] for all actions. We also used the 2D-to-3D pose estimator by Zhou et al. [39] with convex-relaxation as baseline and observed considerable improvement compared to [1] in both 3D pose and projection matrix estimation. Using [39] as baseline to estimate the 3D torso and projection matrix we generated multiple 3D pose hypotheses. Since the performance of [39] was very good, the best out of 5 pose hypotheses achieved only a slightly lower average joint distance compared to the single 3D pose output by [39]. However, by increasing the number of hypotheses we started to observe improvement. Table 1 also includes the best hypothesis out of conditional samples from only the first diversification stage *i.e.*, by diversifying prior samples and using no kmeans++ clustering, using [39] as base. This achieves the lowest joint error in comparison to other baselines. The pose hypotheses can be generated very quickly in only a few seconds in Matlab on an Intel i7-4790K processor with 32-GB RAM.

We also used Deep3D of Chen et al. [10] as another baseline. The Deep3D [10] is a 3D pose estimator that directly regresses to the 3D joint locations directly from a monocular RGB input image. Deep3D had the highest mean joint errors as shown in Table 1. We also observed that the pre-trained Deep3D is very sensitive to image rotation and usually outputs an anatomically implausible 3D pose if the input image is rotated. But other 2D-to-3D pose estimation baselines which decouple the projection matrix and the 3D pose are quite robust to rotation of the input image. Figure 7 shows the Percentage of Correct Keypoints (PCK) versus an acceptance distance threshold in millimeter for various baselines and H36M dataset variation namely the original H36M and 30/60 degree rotations (Figure 9 shows the corresponding PCK curves without bone normalization). One can see that the PCK of Deep3D drops drastically by rotating the input image. This is partly due to insufficient number of tilted samples in the training set (H36M plus synthetic images).

In a realistic scenario with occlusion, the location of some 2D joints cannot be accurately detected. The added

¹<http://www-personal.umich.edu/~alnewell/pose/>

| Method | Directions | Discussion | Eating | Greeting | Phoning | Posing | Purchases | Sitting | SitDown |
|-------------------------|---------------|---------------|---------------|---------------|---------------|---------------|---------------|---------------|---------------|
| Ours (No Kmeans++/[39]) | 63.12 | 55.91 | 58.11 | 64.48 | 68.69 | 61.27 | 55.57 | 86.06 | 117.57 |
| Ours (k=20/[39]) | 77.08 | 71.15 | 75.39 | 79.01 | 84.68 | 74.90 | 72.37 | 102.17 | 131.46 |
| Ours (k=5/[39]) | 82.86 | 77.52 | 81.60 | 85.20 | 90.93 | 80.46 | 78.75 | 109.27 | 138.71 |
| Zhou et al. [39] | 80.51 | 74.56 | 73.95 | 85.43 | 88.96 | 82.02 | 76.21 | 107.43 | 146.47 |
| Ours (k=5/[1]) | 105.14 | 100.28 | 107.75 | 106.88 | 111.44 | 105.74 | 101.18 | 124.87 | 147.48 |
| Akhter&Black [1] | 133.80 | 128.03 | 124.47 | 133.47 | 133.93 | 136.63 | 128.30 | 133.61 | 162.01 |
| Chen et al. [10] | 145.37 | 139.11 | 140.24 | 149.13 | 149.61 | 154.30 | 147.04 | 161.49 | 200.06 |

| | Smoking | TakingPhoto | Waiting | Walking | WalkingDog | WalkTogether | Average |
|-------------------------|---------------|---------------|---------------|---------------|---------------|---------------|---------------|
| Ours (No Kmeans++/[39]) | 71.02 | 71.21 | 66.29 | 57.07 | 62.50 | 61.02 | 67.99 |
| Ours (k=20/[39]) | 85.90 | 84.49 | 80.41 | 71.57 | 78.41 | 74.92 | 82.93 |
| Ours (k=5/[39]) | 91.79 | 90.06 | 86.43 | 77.93 | 85.45 | 81.49 | 89.23 |
| Zhou et al. [39] | 90.61 | 93.43 | 85.71 | 80.03 | 90.89 | 85.73 | 89.46 |
| Ours (k=5/[1]) | 113.61 | 105.58 | 105.80 | 100.28 | 106.25 | 104.63 | 109.79 |
| Akhter&Black [1] | 135.75 | 132.92 | 133.93 | 133.84 | 131.77 | 134.80 | 134.48 |
| Chen et al. [10] | 152.37 | 159.18 | 152.67 | 148.20 | 156.10 | 147.71 | 153.51 |

Table 1: Quantitative comparison on the Human3.6M dataset evaluated in 3D by mean per joint error (mm) for all actions and subjects whose ground-truth 3D poses were provided.

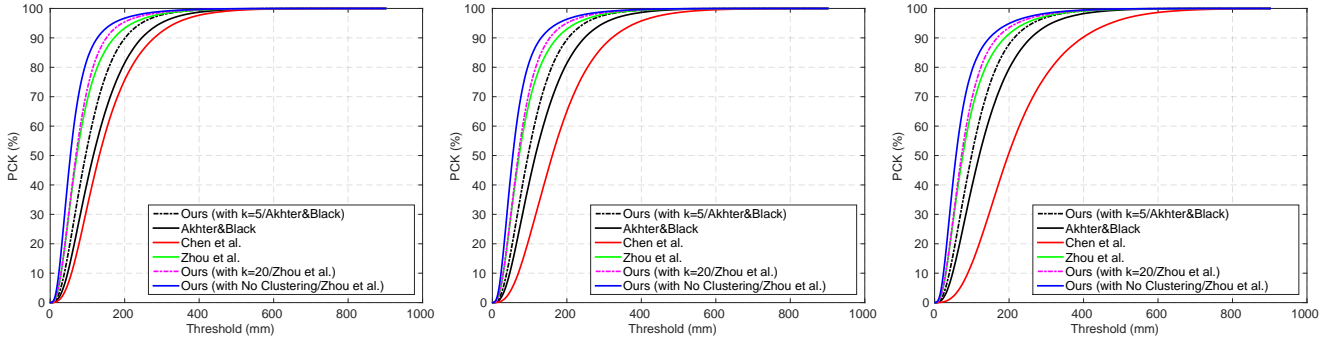


Figure 7: PCK curves for the H36M dataset (original), H36M rotated by 30 and 60 degrees respectively from left to right. The y-axis is the percentage of correctly detected joints in 3D for a given distance threshold in millimeter (x-axis).

uncertainty cause by occlusion makes one expect a larger average estimation error for the estimated 3D pose compared to the best 3D pose hypothesis. To test this, we ran experiments with different number of missing joints (0, 1 and 2) selected randomly from the limb joints including l/r elbow, l/r wrist, l/r knee, and l/r ankle. Table 2 shows the mean per joint errors for the 3D pose estimated by the modified version of Akhter&Black [1] that can handle missing joints compared to the best out of five hypotheses generated by our method when 0, 1, and 2 limb joints are missing. In this test, we used the ground-truth 2D location of the joints and randomly selected the missing joints. Figure 8 illustrates the PCK curves for the missing limb joint experiment. One can see that by increasing the number of missing joints the performance gap between the estimated 3D pose and the best 3D pose hypothesis increases. This underscores the importance of having multiple hypothesis in realistic scenarios.

4. Discussion

In this paper, we proposed a way to generate multiple 3D pose hypotheses consistent with the 2D joint detection in a single-view RGB image. To generate these pose hypotheses we used a flexible and unbiased generative model that only enforces anatomical constraints on the joint-angle limits and limb length ratios. The proposed generative model is compositional (*i.e.* generates a pose by composing the body parts) and spans the full variability of human 3D pose. A system that is not compositional can always suffer from a biased dataset (*e.g.* lack of enough rotated images for the Deep3D method). The number of configurations for an articulated object like the human increases combinatorially by changes in the part locations. The variations of different body shapes, clothing, and camera view points also contribute to the combinatorial growth of 2D images. This signifies the importance of compositionality and the difficulty of dealing with dataset bias if compositionality is not con-

| Method | Directions | Discussion | Eating | Greeting | Phoning | Posing | Purchases | Sitting | SitDown |
|------------------|---------------|---------------|---------------|---------------|---------------|---------------|---------------|---------------|---------------|
| Ours (k=5/[1]) | 98.44 | 93.70 | 102.62 | 97.50 | 96.29 | 98.90 | 93.32 | 105.51 | 110.07 |
| Akhter&Black [1] | 118.02 | 112.55 | 111.27 | 117.46 | 111.77 | 122.27 | 112.23 | 107.27 | 126.95 |
| Ours (k=5/[1]) | 108.60 | 105.85 | 105.63 | 109.01 | 105.47 | 109.93 | 102.01 | 111.25 | 119.57 |
| Akhter&Black [1] | 153.80 | 149.14 | 135.44 | 155.06 | 139.62 | 156.46 | 149.05 | 126.33 | 141.89 |
| Ours (k=5/[1]) | 125.03 | 121.77 | 115.13 | 124.11 | 116.92 | 123.75 | 116.42 | 119.63 | 130.81 |
| Akhter&Black [1] | 185.57 | 180.43 | 158.55 | 185.65 | 162.39 | 185.78 | 178.81 | 145.15 | 155.29 |

| | Smoking | TakingPhoto | Waiting | Walking | WalkingDog | WalkTogether | Average | Average Diff. |
|------------------|---------------|---------------|---------------|---------------|---------------|---------------|---------------|---------------|
| Ours (k=5/[1]) | 97.53 | 97.63 | 99.43 | 90.23 | 97.27 | 95.21 | 98.24 | |
| Akhter&Black [1] | 113.22 | 120.61 | 119.97 | 115.81 | 116.60 | 115.62 | 116.11 | 17.87 |
| Ours (k=5/[1]) | 107.76 | 107.05 | 111.34 | 108.38 | 106.96 | 110.28 | 108.61 | |
| Akhter&Black [1] | 142.98 | 152.65 | 155.27 | 155.18 | 151.88 | 155.00 | 147.98 | 39.37 |
| Ours (k=5/[1]) | 120.60 | 118.38 | 127.13 | 125.89 | 121.61 | 127.62 | 122.32 | |
| Akhter&Black [1] | 165.47 | 177.44 | 186.20 | 189.66 | 183.01 | 186.25 | 175.04 | 52.72 |

Table 2: Quantitative comparison on the Human3.6M dataset when 0 (top pair), 1 (middle pair), and 2 (bottom pair) limb joints are missing. One can see that as the number of missing joints increases the performance gap between the best pose hypothesis and the estimated pose increases as well.

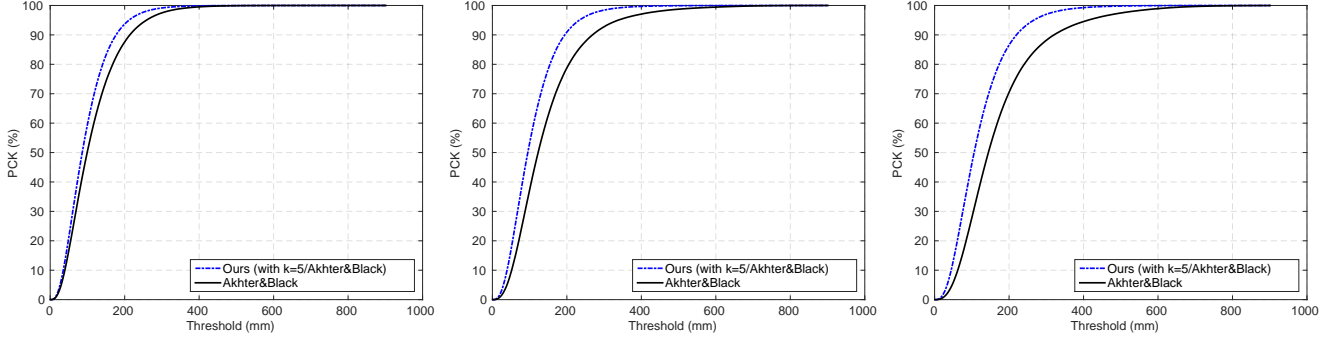


Figure 8: PCK curves calculated on the H36M dataset when 0 (left figure), 1 (middle figure), and 2 (right figure) limb joints are missing. The y-axis is the percentage of correctly detected joints in 3D for a given distance threshold in millimeter (x-axis).

sidered. Handling dataset bias without considering compositionality does not seem logical. On the other hand using a holistic approach can suffer under occlusion where some of the parts are missing whereas a compositional approach can simply ignore occluded parts and make inference based on visible ones.

We discussed both unconditional and conditional sampling given the 2D location of joints. The conditional samples were then clustered to generate a few number of diverse pose hypotheses. There usually exist multiple 3D poses consistent with the 2D location of joints. Hence, there is a level of uncertainty because of losing the depth information in monocular RGB images. The uncertainty increase in the presence of occlusion and imperfect 2D detection of joints. However, most of the existing works on 3D human pose estimation only output one pose hypothesis despite these uncertainties. Considering these uncertainties, we proposed a method to generate multiple pose hypotheses. We performed empirical evaluation on the H36M

dataset and achieved lower mean joint errors for the best pose hypothesis compared to the estimated pose by other recent baselines. The 3D pose output by the baseline methods could also be included as one hypothesis but to investigate our hypothesis generation approach we did not do so in the experimental results. Our experiments show the importance of having multiple 3D pose hypotheses given only the 2D location of joints especially when some of the joints are missing.

The 3D hypotheses can be ranked based on their popularity depending on the activity, physics or more detailed information from the image beyond the 2D location of joints. For example, the middle hypothesis in Figure 5 is in an imbalanced pose not consistent with gravity and therefore can be ranked at the bottom. One simple way to rank a hypothesis is to see how often it gets repeated in a motion capture dataset and rank based on the pose sample frequency; of course this approach will be prone to dataset bias favoring one pose over another. To count a pose from the MoCap

| Method | Directions | Discussion | Eating | Greeting | Phoning | Posing | Purchases | Sitting | SitDown |
|-------------------------|---------------|---------------|---------------|---------------|---------------|---------------|---------------|---------------|---------------|
| Ours (No Kmeans++/[39]) | 74.43 | 66.68 | 67.94 | 75.22 | 77.33 | 70.59 | 64.54 | 95.60 | 127.34 |
| Ours (k=20/[39]) | 85.59 | 79.51 | 81.64 | 87.28 | 90.62 | 82.34 | 78.87 | 108.92 | 138.32 |
| Zhou et al. [39] | 89.06 | 82.67 | 80.59 | 93.48 | 95.59 | 88.41 | 81.86 | 113.95 | 151.62 |
| Ours (k=5/[1]) | 108.63 | 102.85 | 109.09 | 109.77 | 113.19 | 108.18 | 103.51 | 126.18 | 149.31 |
| Akhter&Black [1] | 139.37 | 133.33 | 129.15 | 139.45 | 138.08 | 142.11 | 132.97 | 135.56 | 163.31 |
| Chen et al. [10] | 155.48 | 151.70 | 148.96 | 162.24 | 157.17 | 165.61 | 163.51 | 166.48 | 200.43 |

| | Smoking | TakingPhoto | Waiting | Walking | WalkingDog | WalkTogether | Average |
|-------------------------|---------------|---------------|---------------|---------------|---------------|---------------|---------------|
| Ours (No Kmeans++/[39]) | 79.63 | 79.09 | 73.41 | 67.38 | 71.79 | 72.81 | 77.58 |
| Ours (k=20/[39]) | 92.13 | 89.65 | 85.24 | 80.04 | 85.87 | 84.57 | 90.04 |
| Zhou et al. [39] | 97.25 | 97.32 | 89.98 | 88.53 | 96.84 | 95.33 | 96.17 |
| Ours (k=5/[1]) | 115.74 | 108.56 | 108.99 | 103.32 | 108.01 | 106.92 | 112.15 |
| Akhter&Black [1] | 140.17 | 138.71 | 139.73 | 141.21 | 137.91 | 140.39 | 139.43 |
| Chen et al. [10] | 160.63 | 165.61 | 160.84 | 164.17 | 171.33 | 163.04 | 163.81 |

Table 3: Quantitative comparison on the Human3.6M dataset evaluated in 3D by mean per joint error (mm) for all actions and subjects whose ground-truth 3D poses were provided without bone matching to the 3D ground-truth pose.

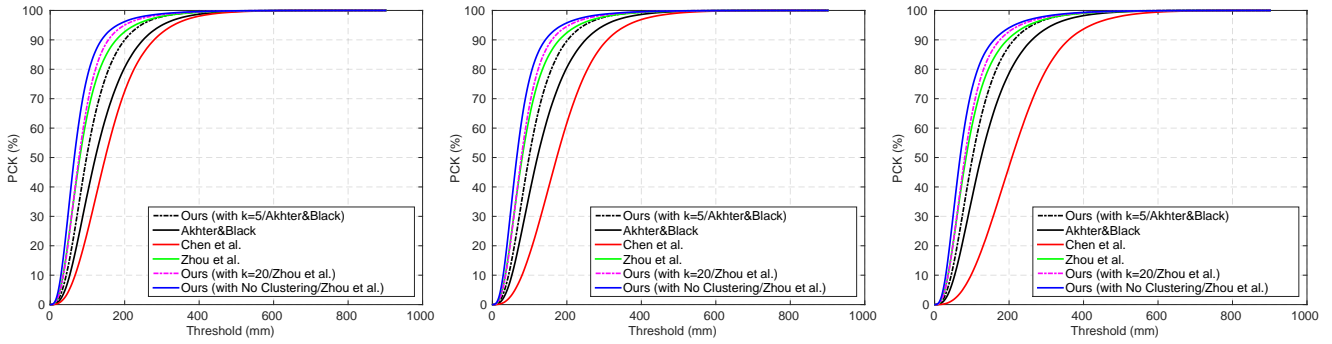


Figure 9: PCK curves for the H36M dataset (original), H36M rotated by 30 and 60 degrees without bone matching to the 3D ground-truth pose respectively from left to right. The y-axis is the percentage of correctly detected joints in 3D for a given distance threshold in millimeter (x-axis).

dataset as positive its distance from the 3D pose hypotheses has to be smaller than a threshold. Another way to rank the hypotheses is to rank them based on their likelihood under a pose model conditional to the scene category (*e.g.* sport field vs indoor), or in the case of interacting people, conditional to the pose of other people in the scene.

5. Acknowledgement

The authors would like to thank Chenxu Luo for his help to run Deep3D pose estimator [10].

References

- [1] I. Akhter and M. J. Black. Pose-conditioned joint angle limits for 3D human pose reconstruction. In *CVPR*, pages 1446–1455, June 2015. [2](#), [3](#), [4](#), [5](#), [6](#), [8](#), [9](#), [10](#), [11](#)
- [2] S. Amin, M. Andriluka, M. Rohrbach, and B. Schiele. Multi-view pictorial structures for 3d human pose estimation. In *British Machine Vision Conference (BMVC)*, September 2013. [3](#)
- [3] M. Andriluka, L. Pishchulin, P. Gehler, and B. Schiele. 2d human pose estimation: New benchmark and state of the art analysis. In *CVPR*, June 2014. [8](#)
- [4] D. Arthur and S. Vassilvitskii. K-means++: The advantages of careful seeding. In *Proceedings of the Eighteenth Annual ACM-SIAM Symposium on Discrete Algorithms, SODA '07*, pages 1027–1035, Philadelphia, PA, USA, 2007. Society for Industrial and Applied Mathematics. [7](#)
- [5] V. Belagiannis, S. Amin, M. Andriluka, B. Schiele, N. Navab, and S. Ilic. 3d pictorial structures for multiple human pose estimation. In *CVPR*, 2014. [3](#), [4](#)
- [6] V. Belagiannis, S. Amin, M. Andriluka, B. Schiele, N. Navab, and S. Ilic. 3d pictorial structures revisited: Mul-

- multiple human pose estimation. *IEEE Transactions on Pattern Analysis and Machine Intelligence*, 38(10):1929–1942, 2016. 3
- [7] F. Bogo, A. Kanazawa, C. Lassner, P. Gehler, J. Romero, and M. J. Black. Keep it smpl: Automatic estimation of 3d human pose and shape from a single image. In *ECCV*, 2016. 3
- [8] A. Bulat and G. Tzimiropoulos. Human pose estimation via convolutional part heatmap regression. In *ECCV*, 2016. 3
- [9] M. Burenius, J. Sullivan, and S. Carlsson. 3d pictorial structures for multiple view articulated pose estimation. In *CVPR*, pages 3618–3625, 2013. 3
- [10] W. Chen, H. Wang, Y. Li, H. Su, Z. Wang, C. Tu, D. Lischinski, D. Cohen-Or, and B. Chen. Synthesizing training images for boosting human 3d pose estimation. In *3D Vision (3DV)*, 2016. 2, 3, 8, 9, 11
- [11] X. Chen and A. L. Yuille. Articulated pose estimation by a graphical model with image dependent pairwise relations. In *Advances in Neural Information Processing Systems*, pages 1736–1744, 2014. 3
- [12] X. Chu, W. Ouyang, H. Li, and X. Wang. Structured feature learning for pose estimation. In *CVPR*, 2016. 3
- [13] P. Doe. Cmu human motion capture database. available online at:, 2003. 2, 4
- [14] M. Eichner, M. Marin-Jimenez, A. Zisserman, and V. Ferrari. 2d articulated human pose estimation and retrieval in (almost) unconstrained still images. *International Journal of Computer Vision*, 99:190–214, 2012. 3
- [15] M. Everingham, S. M. A. Eslami, L. Van Gool, C. K. I. Williams, J. Winn, and A. Zisserman. The pascal visual object classes challenge: A retrospective. *International Journal of Computer Vision*, 111(1):98–136, Jan. 2015. 5
- [16] E. Insafutdinov, L. Pishchulin, B. Andres, M. Andriluka, and B. Schiele. Deepcrut: A deeper, stronger, and faster multi-person pose estimation model. In *ECCV*, May 2016. 5
- [17] C. Ionescu, D. Papava, V. Olaru, and C. Sminchisescu. Human3.6m: Large scale datasets and predictive methods for 3d human sensing in natural environments. *IEEE Transactions on Pattern Analysis and Machine Intelligence*, 36(7):1325–1339, jul 2014. 2, 8
- [18] E. Jahangiri, E. Yoruk, R. Vidal, L. Younes, and D. Geman. Information pursuit: A bayesian framework for sequential scene parsing. *arXiv:1701.02343*, 2017. 4
- [19] A. M. Lehrmann, P. V. Gehler, and S. Nowozin. A non-parametric bayesian network prior of human pose. In *CVPR*, pages 1281–1288, 2013. 2, 4
- [20] S. G. Mallat and Z. Zhang. Matching pursuits with time-frequency dictionaries. *IEEE Transactions on Signal Processing*, pages 3397–3415, Dec. 1993. 4
- [21] A. Newell, K. Yang, and J. Deng. Stacked hourglass networks for human pose estimation. In *ECCV*, May 2016. 2, 3, 4, 5, 6, 7, 8
- [22] L. Pishchulin, E. Insafutdinov, S. Tang, B. Andres, M. Andriluka, P. Gehler, and B. Schiele. Deepcut: Joint subset partition and labeling for multi person pose estimation. In *CVPR*, June 2016. 5
- [23] G. Pons-Moll, D. J. Fleet, and B. Rosenhahn. Posebits for monocular human pose estimation. In *CVPR*, pages 2345–2352, June 2014. 4
- [24] V. Ramakrishna, T. Kanade, and Y. Sheikh. Reconstructing 3d human pose from 2d image landmarks. In *ECCV*, 2012. 3, 4
- [25] G. Rogez and C. Schmid. Mocap-guided data augmentation for 3d pose estimation in the wild. 2016. 3
- [26] B. Sapp and B. Taskar. Modec: Multimodal decomposable models for human pose estimation. In *CVPR*, pages 3674–3681, 2013. 3, 5, 8
- [27] L. Sigal, A. Balan, and M. J. Black. Humaneva: Synchronized video and motion capture dataset and baseline algorithm for evaluation of articulated human motion. *International Journal of Computer Vision*, 87:4–27, 2010. 2
- [28] L. Sigal, M. Isard, H. Haussecker, and M. J. Black. Loose-limbed people: Estimating 3D human pose and motion using non-parametric belief propagation. *International Journal of Computer Vision*, 98(1):15–48, May 2011. 3
- [29] E. Simo-Serra, A. Quattoni, C. Torras, and F. Moreno-Noguer. A joint model for 2d and 3d pose estimation from a single image. In *CVPR*, pages 3634–3641, 2013. 4
- [30] E. Simo-Serra, A. Ramisa, G. Alenyà, C. Torras, and F. Moreno-Noguer. Single image 3d human pose estimation from noisy observations. In *CVPR*, 2012. 3
- [31] J. J. Tompson, A. Jain, Y. LeCun, and C. Bregler. Joint training of a convolutional network and a graphical model for human pose estimation. In *Advances in neural information processing systems*, pages 1799–1807, 2014. 3
- [32] A. Toshev and C. Szegedy. Deeppose: Human pose estimation via deep neural networks. In *CVPR*, pages 1653–1660, 2014. 3
- [33] L. van der Maaten and G. E. Hinton. Visualizing high-dimensional data using t-sne. *Journal of Machine Learning Research*, 9:2579–2605, 2008. 2
- [34] C. Wang, Y. Wang, Z. Lin, A. L. Yuille, and W. Gao. Robust estimation of 3d human poses from a single image. In *CVPR*, 2014. 3
- [35] S.-E. Wei, V. Ramakrishna, T. Kanade, and Y. Sheikh. Convolutional pose machines. In *CVPR*, June 2016. 3
- [36] H. L. X. W. Xiao Chu, Wanli Ouyang. Crf-cnn: Modeling structured information in human pose estimation. In *NIPS*, 2016. 3
- [37] W. Yang, W. Ouyang, H. Li, and X. Wang. End-to-end learning of deformable mixture of parts and deep convolutional neural networks for human pose estimation. In *CVPR*, 2016. 3
- [38] Y. Yang and D. Ramanan. Articulated pose estimation with flexible mixtures-of-parts. In *CVPR*, 2011. 3
- [39] X. Zhou, S. Leonardos, X. Hu, and K. Daniilidis. 3d shape estimation from 2d landmarks: A convex relaxation approach. In *CVPR*, pages 4447–4455, June 2015. 2, 3, 4, 5, 6, 8, 9, 11
- [40] X. Zhou, M. Zhu, S. Leonardos, K. G. Derpanis, and K. Daniilidis. Sparseness meets deepness: 3d human pose estimation from monocular video. In *CVPR*, June 2016. 3